43rd AIAA Thermophysics Conference
25 - 28 June 2012, New Orleans, Louisiana

AIAA 2012-3002

Analysis of High-enthalpy Air-chemistry and its Effect on Stagnation Point Heat Flux

D. Siva K. Reddy * and Krishnendu Sinha †
Indian Institute of Technology Bombay, Mumbai, 400076, India.

Abstract

The present work studies the non-equilibrium chemical reactions occurring in a re-entry flow with a stagnation enthalpy of 31.53 MJ/kg. The objective is to investigate the chemical and physical processes in different regions of the flowfield, and their effect on the stagnation point heat flux. Numerical experiments are performed by altering the reaction rates from their baseline values and the computed flowfield solutions are analyzed in detail. The primary chemical activity consists of dissociation of N and O in the shock layer, and recombination of only N atoms in the vicinity of the isothermal cold wall. The reaction mechanisms involved in the conversion of N atoms to molecules are presented and the rate limiting steps are identified. The surface heat flux is found to be most sensitive to these rate constants. Increasing their values enhances the heat transfer rate and vice versa. The study also highlights the effect of shock layer chemistry and chemical non-equilibrium on the surface predictions. Most importantly, the analysis explains why the heating rate is sensitive to some of the rate constants and relatively insensitive to other reaction rates.

Nomenclature

D	diameter of the vehicle, m
k_f	forward reaction rate coefficient, $m^3/(kg\text{-}mol.s)$
k_b	backward reaction rate coefficient, $m^3/(kg\text{-}mol.s)$ or $m^6/(kg\text{-}mol^2.s)$
K_{eq}	equilibrium constant
l	wall normal distance, m
M	Mach number or molecular weight, kg/kg-mol
p	pressure, Pa
q	heat transfer rate, W/cm^2
R	net reaction rate for a chemical reaction, $kg\text{-}mol/(m^3.s)$
s	arc length measured from nose stagnation point, m
U	velocity, m/s
Y	species mass fraction
T	translational-rotational temperature, K
T_v	vibrational temperature, K
T_a	geometrically-averaged temperature, K
H_o	total enthalpy of the flow, MJ/kg
C_f and η	coefficients for the calculation of a chemical reaction rate
θ_d	characteristic temperature for a chemical reaction
ρ	density, kg/m^3
μ	molecular viscosity, Pa.s
κ	thermal conductivity, W/m.K
δ	thermal boundary layer thickness, m

Subscripts

2	cell next to the wall in the computational grid
i	species number

*Doctoral student, Department of Aerospace Engineering.
†Associate Professor, Department of Aerospace Engineering, Senior AIAA Member.

n	reaction number
w	wall
∞	freestream

Abbreviations

CFD	computational fluid dynamics
rsf	reaction scaling factor
FIRE	flight investigation re-entry experiment

I. Introduction

Re-entry flowfields are characterized by high-temperature effects such as excitation of internal energy modes, chemical reactions, ionization and radiation. These high-temperature phenomena have a dominant effect on the aero-thermodynamics of re-entry vehicles. For example, heat released or absorbed during chemical reactions affects the temperature of the gas. This in turn affects the surface heat flux, which is the primary input to the design of heat shields. Also, the shock stand-off distance on a blunt-nose configuration is determined by the density rise across the shock wave. This in turn is a function of the free-stream Mach number and the degree of chemical reactions in the post-shock flow. A comparison of the shock stand-off distance against experimental visualization is often used to evaluate the accuracy of chemical kinetic models used in numerical simulation of high-enthalpy flows.

The chemical reactions alter the gas composition, and the associated properties like conductivity and viscosity of the gas mixture. Changes in conductivity of the fluid medium has first order effect on the heat transfer rates. Variation in fluid viscosity affects the local Reynolds number and thus can alter flow separation characteristics, for example, on the afterbody of a re-entry capsule. This may change the pressure distribution on the afterbody frustum, leading to an increase or decrease of the aerodynamic moments for non-zero angles of attack. Further, the size of localized separation bubbles in viscous-inviscid interactions, for example, on a double-cone configuration,[1] are found to be sensitive to the chemical reactions in the flow. Changes in separation and reattachment locations alter the associated shock structure, and thus affect the pressure distribution significantly. Such viscous-inviscid interaction flows often occur on control surfaces, and the chemical reactions occurring in the gas can alter their effectiveness.[2]

Thus, chemical reactions affect re-entry flows in multiple ways and a detailed understanding of the chemistry and its effects on flow features is important. A study of the underlying physical mechanisms is required so that we can identify the critical factors through which chemistry interacts with the flow. Such insight can help explain high-enthalpy flow phenomena observed in flight, in ground-based experiments, and in computational investigations. Most importantly, it can give valuable information regarding the sensitivity of numerical predictions of aero-thermal loads to uncertainty in chemical rate constants used in the simulations.

The gas-phase chemistry at re-entry conditions usually consists of multiple dissociation/recombination and exchange reactions. The rate of these reactions depends on the temperature and pressure of the gas mixture, and therefore vary from point to point in a re-entry flowfield. The reaction rates are also function of the molar concentration of different species in the gas mixture. The gas dynamic and diffusion processes in the flow determine the local gas properties, and thus have a major role to play in determining the chemical activity in a region. The chemical reactions, in turn, alter the local gas properties, and thus can have significant effect on the gas dynamics and heat transfer, as discussed above. Thus, there is a two-way inter-dependence between the flow processes and the chemical reactions occurring at re-entry conditions.

The thermo-chemical processes occurring in the gas require a finite number of molecular/atomic collisions to reach equilibrium. At flight conditions, the gas density is usually too low to induce enough collisions to reach equilibrium as the gas passes through the shock layer. The chemistry time scales are often comparable to the fluidynamic times scales, leading to significant non-equilibrium effects in re-entry flows. The degree of thermo-chemical non-equilibrium depends on the gas density, which varies over a large range in the flow around a re-entry capsule. The gas density increases by an order in magnitude across the shock wave and further increases in the vicinity of an isothermal wall. On the other hand, flow expansion around the shoulder results in very low density on the afterbody. The local chemical state of the gas, therefore, is a function of not only the chemical reactions, but also the extent of chemical non-equilibrium at the given thermodynamic

Freestream Conditions	Higher altitude	Lower altitude
Altitude (km)	70	35
ρ_∞ (kg/m^3)	0.000152	0.0083
U_∞ (m/s)	7920	4950
T_∞ (K)	227	237
M_∞	26.2	16
$Re_{\infty D}$	4.79 $\times 10^4$	1.76 $\times 10^6$
H_0 (MJ/kg)	31.53	12.5

Table 1: Freestream conditions for the current simulations (70 km altitude) and the lower altitude conditions used in Ref. 5.

condition of the gas. Understanding the effects of multiple parameters, like temperature, density and gas composition, which vary from point to point in a re-entry flow is a challenging task.

The objective of this work is to analyze the chemical reactions occurring in a high-enthalpy re-entry flowfield and study its effect on the aerothermodynamics of a re-entry capsule. The current paper focuses on the stagnation point heat transfer rate. A companion paper[3] studies the thermo-chemical effects at different locations around a capsule geometry. The freestream conditions correspond to 70 km altitude point of AS-202 re-entry trajectory point[4] (4500 sec after launch) and are listed in Table 1. A similar study at a low altitude condition (35 km altitude of FIRE II trajectory; 1652.75 sec after launch) was presented in Ref. 5 and freestream conditions at this point are also listed in the table.

We use CFD as a tool to study the thermo-chemistry and its interaction with the fluid dynamic and heat transfer processes at the chosen re-entry conditions. Flowfield solution is obtained using a five-species air chemistry with reaction rates taken from Ref. 6. These kinetic data are routinely used in re-entry flow calculations. The computed solution is analyzed in detail in terms of the variation in gas temperature, density and composition over the entire flowfield. How these gas properties determine the local chemistry and the degree of non-equilibrium is studied next. The rates of different chemical reactions and the resulting species source terms are compared to identify the dominant chemical reactions and the reaction mechanisms occurring in the flow. The net effect of the reactions on the flowfield can be observed by studying the variation in gas composition, and the associated properties.

Next, controlled numerical experiments are performed by varying the reaction rates and studying their effect on the flow processes. The rate constants of the chemical reactions are altered either individually or in groups. Based on an understanding of the baseline chemistry, specific cases are identified for detailed analysis. Comparison of the altered reactivity simulations with the baseline solution provides valuable information about the chemical activity in the flowfield. It allows us to evaluate the contribution of individual reactions, and of competing reaction mechanisms to the overall changes in the gas composition. The rate-limiting steps in the different reaction mechanism are also identified.

The variation in chemical rate constants in the altered reactivity simulations is based on experimental uncertainty in these parameters. Park reports uncertainty up to an order of magnitude in the reaction rate constants (see for example, Fig. 8.2 in Ref. 6). Sensitivity and uncertainty analysis of re-entry flow predictions vary the kinetic parameters in this range and perform a large number of simulations to quantify their effect on quantities of practical interest, like, the surface heat transfer.[7,8] The current work also studies the effect of variation in chemical reaction rates on aero-thermal predictions, but is different from sensitivity analysis in two major aspects. First, we do not cover the entire range of the reaction rate constant values. In stead, carefully chosen limiting cases are considered to study the underlying mechanisms via which the chemistry influences the flow predictions. Second, the current study provides qualitative information on how the aero-thermal predictions depend on a specific reaction rate. This is in contrast to regular sensitivity analysis which use a distribution function to vary the rate constants and calculate quantitative data for the sensitivity of the computational predictions to the uncertainty in kinetic parameters.

Note that the focus of the current paper is on the gas-phase chemistry in high-enthalpy air, and its effect on the stagnation point heating rate. The effect of other thermo-chemical processes like, surface catalysis, vibrational relaxation and species diffusion, on the surface heat flux is not part of this study. As a result, the variation in heat flux values reported here do not include competing effects due to uncertainties in catalytic parameters and diffusion coefficients, and should therefore be interpreted with caution. In spite of this

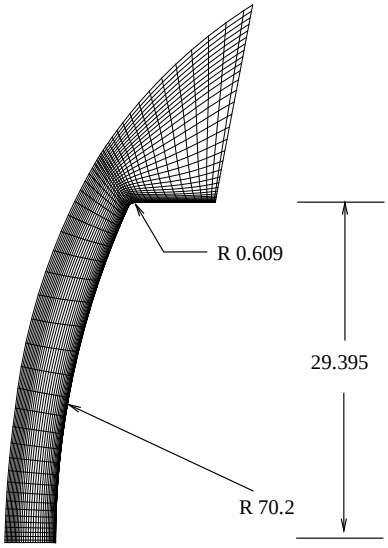

Figure 1: Geometry and computational grid used in the simulations. Every second point is shown in each direction. The vehicle dimensions are in cm.

limitation, the present analysis yields valuable insight into the thermo-chemistry occurring in the stagnation region of a re-entry flowfield. The paper answer a key question, why the surface heating rate is sensitive to some chemical rate constants and relatively insensitive to other reaction rates. This is the focus of the current work.

II. Simulation Methodology

The chemically reacting hypersonic flow is simulated by solving the Navier-Stokes equations along with the species conservation equations and a thermal non-equilibrium model. Air is modeled as a neutral mixture of five perfect species (N_2, O_2, NO, N and O) with three dissociation and two exchange reactions. The two-temperature model of Park[6] is used to describe thermal state of the gas. An additional conservation equation is solved for vibrational energy of the mixture to account for the thermal non-equilibrium. The Arrhenius rate constants for the chemical reactions are evaluated using curve fits to experimental data by Park.[6] The molecular viscosity of each species is determined using curve fit data of Blottner *et al.*[10] Thermal conductivities for the translational and rotational modes of the species are then determined using the Eucken relation.[11] Viscosity and thermal conductivity of the mixture are computed by employing Wilke's mixing rule.[12] Multi-component mass diffusion due to concentration gradient is modeled using Fick's law with a Lewis number of 1.4.

The axisymmetric form of the governing equations is discretized using the finite-volume method. Inviscid fluxes are computed using a modified (low-dissipation) form of the Steger-Warming flux splitting approach.[13] The method is second-order accurate in both streamwise and wall-normal directions. The viscous fluxes are evaluated using second-order accurate central differencing, and the implicit data parallel line relaxation method[14] is used to obtain steady-state solutions. The code has been used extensively in high-speed flow computations[15,16] and validated against flight data for re-entry conditions.[17]

No-slip, non-catalytic and isothermal boundary conditions are specified at the wall. The temperature of the wall is assumed to be 553.3 K, and is same as that used in the lower altitude simulations.[5] The vibrational temperature is assumed to equilibriate with the translational temperature at the wall. Freestream conditions are applied at the outer boundary and extrapolation condition is imposed at the exit station. Since the freestream Reynolds number based on body diameter is 4.79×10^4, laminar simulations are performed.

The level of ionization in the flowfield is of the order of 0.03 % as reported in Ref. 4. This level of ionization has negligible effect on the flowfield and heat flux. For air temperatures above 10000 K, Wilke's

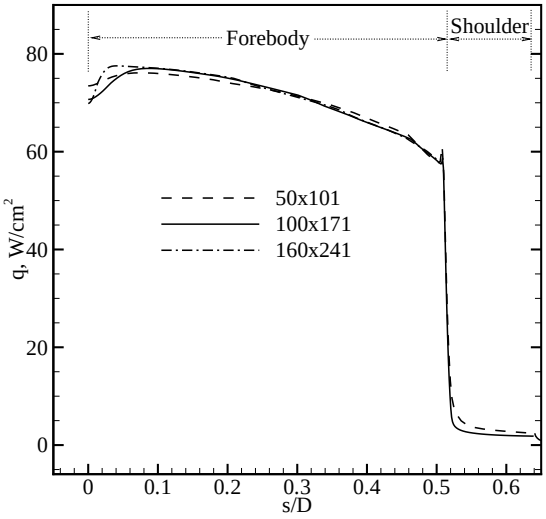

Figure 2: Effect of successive grid refinement on the computed heat flux.

mixing rule is not an accurate approximation to compute the mixture transport properties. The foucs of the paper is to understand the chemistry effects rather than validating the CFD predictions against experimental data. Any error due to the above two modeling assumptions are not expected to alter the qualitative trends reported in the present work. Therefore we use neutral air assumption along with Wilke's mixing rule to compute the flowfield.

A typical grid used in the simulation is shown in Fig. 1. The grid in the wall-parallel direction is designed such that points are clustered in the nose stagnation region and at the shoulder expansion corner. The wall-normal grid is refined both in the vicinity of the shock wave as well as in the near-wall region. In addition, the outer boundary is carefully tailored to the bow shock wave.

A. Grid Refinement Study

Simulations are performed on successively refined grids to assess the sensitivity of the computed solution to the grid-point density. Grid independence is evaluated in terms of the predicted surface heat flux, and tolerance levels are reported below. Figure 2 shows the surface heat flux computed on three meshes, where the number of wall-parallel grid points vary from 50 to 160. In the wall-normal direction, the three grids have 101, 171 and 241 points respectively. The surface heat flux is plotted as a function of the normalized arc length (s/D) measured from the nose stagnation point. There is a noticeable difference between the first two grid solutions, both on the forebody and shoulder. By comparison, the heat transfer rates obtained from the two finer grids (100×171 and 160×241) are almost identical, except for the nose stagnation region ($s/D < 0.1$).

All the solutions show a dip in the heating rate near $s/D = 0$. This non-physical effect is due to the numerical errors caused by a mis-alignment of grid lines to the bow shock contours. Saunders *et al.*[18] propose an algorithm to tailor the grid lines to the bow shock in order to eliminate the irregularity in the predicted heat flux. Starting with an initial grid and the corresponding solution, the algorithm generates a new grid by re-distributing the points so that the grid lines are better aligned to the bow shock. Simulations are performed on the modified grid, and the alignment procedure is repeated until the non-physical variation in heating rate is completely eliminated.

We use the above algorithm to rectify the heat flux variation in the nose stagnation region. Repeated application of the algorithm on the baseline grid (100×171) leads to a relatively monotonic variation of heating rate in the stagnation region, and the corresponding solution is marked as the grid-aligned solution in Fig. 3. Further improvement in heat flux prediction at the stagnation point is achieved by additional grid refinement (by a factor of two in the wall-parallel direction) and repeated alignment to the bow shock. One of the best results from the fine mesh simulations is presented as the benchmark solution and is used for further comparison.

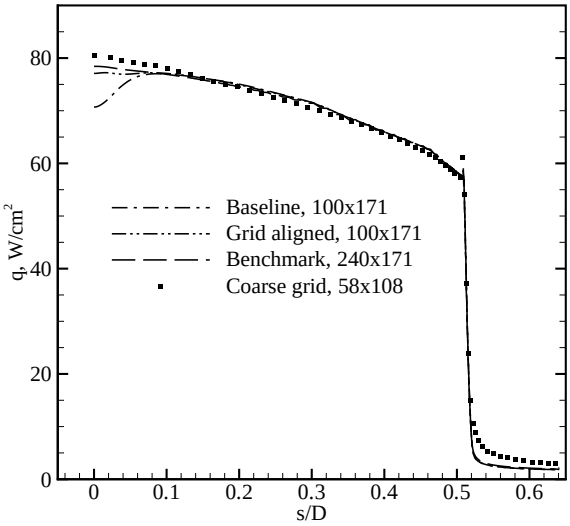

Figure 3: Effect of aligning the grid lines to the shock wave on stagnation point heating rate.

For all the grids presented above, the wall-parallel grid spacing at the nose stagnation point is about 0.1 cm. Achieving a smooth variation in heating rate at the nose stagnation point for such a grid requires many grid-alignment iterations. This process is cumbersome and highly time consuming, when applied for all the altered reactivity simulations presented below. It is found that a mesh with much larger wall-parallel grid spacing (approximately 0.9 cm) at the nose results in a lower sensitivity of the computed solution to the grid-shock mis-alignment. Heating rate obtained from such a coarse grid simulation, with 58 wall-parallel grid points, is shown in Fig. 3. It is fairly monotonic in the stagnation region ($s/D < 0.1$), even without extensive grid alignment. The coarse mesh heating rate prediction compares reasonably well with that of the benchmark solution, with a maximum deviation of about 2.5% at the stagnation point. We choose the coarse mesh (58×108) for further simulations because of its robustness. The wall-normal spacing is 1×10^{-6} m and the corresponding cell Reynolds number is 0.83 or less.

B. Chemical Reaction Kinetics

The five chemical reactions considered in the present work are

$$\mathrm{N_2 + M \rightleftharpoons 2N + M} \tag{1}$$

$$\mathrm{O_2 + M \rightleftharpoons 2O + M} \tag{2}$$

$$\mathrm{NO + M \rightleftharpoons N + O + M} \tag{3}$$

$$\mathrm{N_2 + \ O \rightleftharpoons NO + N} \tag{4}$$

$$\mathrm{NO + O \rightleftharpoons O_2 + N} \tag{5}$$

The first three reactions represent dissociation of molecular nitrogen, oxygen and nitric oxide. M is the collision partner, which provides the required energy to break the chemical bond. The collision partner can be any of the five species, and it remains unaltered in the reaction. The last two reactions are the Zeldovich exchange reactions, which govern the concentration of NO in hypersonic flows. In the following, the five reactions are referred to as per the above numbers and their corresponding reaction rates are given by

$$\begin{aligned} R_1 &= \textstyle\sum_{m=1}^{5} \left[k_{b_{1m}} \frac{\rho_\mathrm{N}}{M_\mathrm{N}} \frac{\rho_\mathrm{N}}{M_\mathrm{N}} \frac{\rho_m}{M_m} - k_{f_{1m}} \frac{\rho_{\mathrm{N_2}}}{M_{\mathrm{N_2}}} \frac{\rho_m}{M_m} \right] \\ R_2 &= \textstyle\sum_{m=1}^{5} \left[k_{b_{2m}} \frac{\rho_\mathrm{O}}{M_\mathrm{O}} \frac{\rho_\mathrm{O}}{M_\mathrm{O}} \frac{\rho_m}{M_m} - k_{f_{2m}} \frac{\rho_{\mathrm{O_2}}}{M_{\mathrm{O_2}}} \frac{\rho_m}{M_m} \right] \\ R_3 &= \textstyle\sum_{m=1}^{5} \left[k_{b_{3m}} \frac{\rho_\mathrm{N}}{M_\mathrm{N}} \frac{\rho_\mathrm{O}}{M_\mathrm{O}} \frac{\rho_m}{M_m} - k_{f_{3m}} \frac{\rho_{\mathrm{NO}}}{M_{\mathrm{NO}}} \frac{\rho_m}{M_m} \right] \end{aligned} \tag{6}$$

$$R_4 = k_{b_4} \frac{\rho_{\rm NO}}{M_{\rm NO}} \frac{\rho_{\rm N}}{M_{\rm N}} - k_{f_4} \frac{\rho_{\rm N_2}}{M_{\rm N_2}} \frac{\rho_{\rm O}}{M_{\rm O}}$$

$$R_5 = k_{b_5} \frac{\rho_{\rm O_2}}{M_{\rm O_2}} \frac{\rho_{\rm N}}{M_{\rm N}} - k_{f_5} \frac{\rho_{\rm NO}}{M_{\rm NO}} \frac{\rho_{\rm O}}{M_{\rm O}}$$

In the preceding equations subscript m indicates collision partner. M_i and ρ_i represent the i^{th} species molecular weight and density respectively. The parameters k_b and k_f are Arrhenius rate constants for backward and forward reactions respectively, and are given by[6]

$$k_{f_n}(T_a) = C_{fn} T_a^{\eta_n} \exp\left(\theta_{dn}/T_a\right) \qquad \text{for } n = 1, ..., 5 \tag{7}$$

where C_{fn}, η_n and θ_{dn} are experimentally determined curve fit data for the n^{th} reaction over a given temperature range. T_a is the effective temperature, and for dissociation reactions ($n = 1,\ 2,\ 3$), it is taken as the geometric average of the translational-rotational and vibrational temperature, *i.e.* $T_a = \sqrt{TT_v}$. For exchange reactions, $T_a = T$. The backward reaction rate constants are obtained using the principle of detailed balance:

$$k_{b_n}(T) = \frac{k_{f_n}(T)}{K_{eq,n}}, \tag{8}$$

where the equilibrium constant $K_{eq,n}$ is given in Ref. 2. The above set of equations define the chemical kinetics used in the current CFD algorithm. The procedure used in the altered reactivity simulations is identical to that in Ref. 6 and is repeated below for completeness.

The data presented in Ref. 6 show that the uncertainty in the measurement of rate constants is about one order of magnitude. Hence, simulations are performed by increasing and decreasing the chemical reaction rate constants (k_f and k_b) by a factor of ten as compared to the baseline values. We change the rate constants for both the forward and backward reactions so that the equilibrium constant remains the same for a given local thermodynamic condition. Similar procedure has been used in Ref. 19.

In the CFD algorithm, the reaction rates are altered by multiplying the rate constants by a reaction scaling factor (rsf). The modified forward rate constant at each point is given by rsf$\times k_{f_n}$, where k_{f_n} is calculated using Eq. (7). The backward reaction rates are also multiplied by the same factor. Hence, a value of rsf = 10 corresponds to higher reactivity simulation, where the reaction rate constants are increased by ten times. On the other hand, rsf = 0.1 represents lower reactivity case, where the reaction rate constants are decreased by ten times; rsf = 1 indicates baseline simulation.

The surface heat transfer rate is directly influenced by gas composition and temperature in the thermal boundary layer adjacent to the wall. The gas properties in this region are primarily determined by the exothermic recombination reactions. On the other hand, the thermo-chemical reactions at the shock wave and in the inviscid shock layer are usually endothermic. Variation in the corresponding reaction rates can alter the boundary-layer edge conditions, and therefore, the surface heating rate predictions.

We first study the sensitivity of surface heat flux to the variations in reaction rates only in the boundary layer. In the baseline simulation, the maximum boundary-layer thickness is found to be 7 mm, which corresponds to about 65 wall-normal points in the computational grid. In this region, the reaction rates are altered by setting rsf $\neq 1$. Outside the boundary layer, a value of rsf = 1 is used, such that the reaction rates match the baseline values. This results in boundary-layer edge conditions that are identical to the baseline solution, and the variation in surface properties is primarily due to altered reactivity in the near-wall region. Variation in fluid properties at the boundary-layer edge, caused by the thermo-chemistry at the shock wave, are subsequently studied by altering the reaction rates uniformly over the entire computational domain. A controlled study of this nature allows us to isolate the physical effects in different parts of the flowfield.

III. Results

A brief description of the computed re-entry flowfield and surface properties is given below. Next, the details of thermo-chemical state of the gas and chemical reactions in the boundary layer are presented. The effect of variation in the chemical reaction rates on heat flux predictions is explained subsequently.

Figure 4 shows the computed flowfield in terms of Mach number distribution. The prominent features of the flowfield, like bow shock and flow expansion, are identified. The boundary layer formed on the forebody is not visible on the scale of the figure. The boundary layer thickness increases across the expansion fan, and

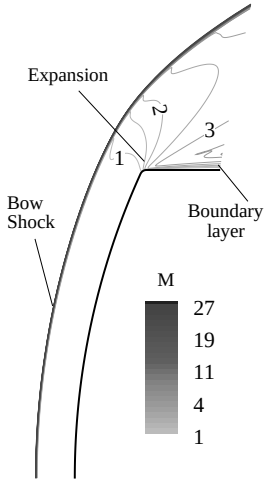

Figure 4: Computed Mach number distribution around the forebody of a re-entry capsule at Mach 26.2.

the Mach number variation in the shoulder boundary layer can be seen near the exit station. The flow on the forebody is subsonic, with Mach number approaching unity close to the expansion corner. The post-shock temperature in the nose stagnation region is about 7000 K. Flow expansion at the shoulder reduces the temperature to 1000 K and the Mach number increases to about 3.

A. Boundary Layer Thermo-Chemistry

The variation of gas temperatures in the thermal boundary layer at the nose stagnation point is presented in Fig. 5(a). Local boundary-layer thickness is used to non-dimensionalize the wall-normal distance. Hence $l/\delta = 0$ represents the vehicle surface and $l/\delta = 1$ corresponds to the boundary-layer edge. Flow is in thermal equilibrium ($T \simeq T_v$) at the edge of the boundary layer, with both translational and vibrational temperatures around 6560 K. In the boundary layer, both temperatures decrease monotonically to reach the wall value of 553.5 K.

The freestream gas is composed of oxygen and nitrogen molecules, with mass fractions of 0.233 and 0.767 respectively. The high temperature of the gas in the shock layer causes complete dissociation of the oxygen molecules and a partial dissociation of the nitrogen molecules. As a result, mass fraction of N_2, N and O species attain values of 0.23, 0.54 and 0.23 respectively at the boundary-layer edge (see Fig. 5(b)). Concentrations of the remaining two species are negligible. The decrease of gas temperature in the boundary layer initiates chemical reactions. As a result, mass fraction of N_2 increases to 0.52 at the wall with a corresponding decrease in Y_N. However, Y_O, Y_{O_2} and Y_{NO} remain constant throughout the boundary layer. The change in gas composition across the boundary layer is explained below with the aid of Fig. 6, which depicts the chemical reaction rates and the species source terms in the boundary layer.

The chemical reactions and associated source terms are effective in the vicinity of the wall ($l/\delta < 0.05$, *i.e.* 5% of the boundary-layer thickness). However, the concentrations of N_2 and N change throughout the boundary layer due to mass diffusion. The largest reaction rate corresponds to NO recombination (see Fig. 6(a)).

$$R_3 > 0 \qquad \mathrm{N + O + M \rightarrow NO + M}$$

The newly created NO molecules collide with the available N atoms to form N_2 molecules through exchange reaction (4)

$$R_4 > 0 \qquad \mathrm{NO + N \rightarrow N_2 + O}$$

For $l/\delta > 0.005$, it is seen that $R_3 \simeq R_4$, and therefore the net effect of the above two reactions is $2N \rightarrow N_2$ with negligible influence on O_2, O and NO. This results in equal and opposite source terms for N_2 and N (see Fig. 6(b)), and the other source terms (for O_2, O and NO) are approximately zero. The reaction rates R_3 and R_4 attain peak value at $l/\delta \approx 0.004$ leading to maximum W_{N_2} and minimum W_N at this location.

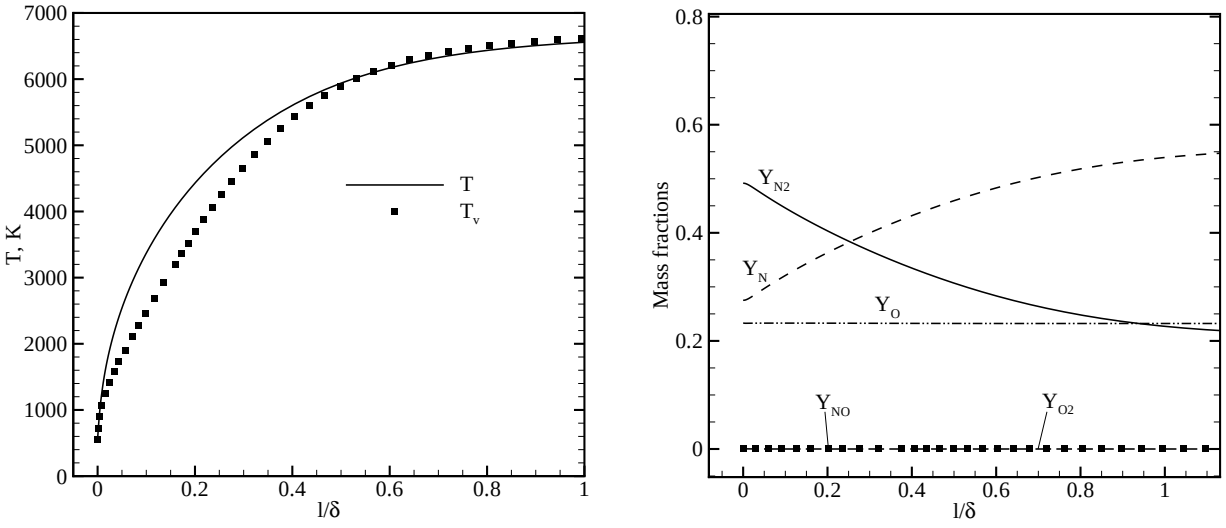

(a) (b)

Figure 5: Distribution of (a) temperatures and (b) species mass fraction in the thermal boundary layer at the nose stagnation point.

A local peak in the source term of N_2 is also observed at $l/\delta \sim 0.012$, which is due to non-zero R_1 in this region.

Availability of NO molecules is critical for continuation of the exchange reaction. As R_3 drops to negligible values for $l/\delta < 0.004$, the magnitude of R_4 decreases (see Fig. 6(a)). For $0 < l/\delta < 0.004$, R_2 and R_5 attain non-negligible values and provide the NO required for reaction (4). The resulting reaction mechanism that leads to the recombination of N atoms is as follows. First, the recombination of oxygen atoms occurs via

$$R_2 > 0 \qquad \mathrm{O + O + M \rightarrow O_2 + M}$$

The newly formed oxygen molecules collide with N atoms, as per reaction (5), resulting in the formation of NO and O atoms

$$R_5 > 0 \qquad \mathrm{O_2 + N \rightarrow NO + O}$$

The newly created NO molecules collide with the available N atoms to form N_2 molecules via reaction (4)

$$R_4 > 0 \qquad \mathrm{NO + N \rightarrow N_2 + O}$$

The two exchange reactions (5) and (4) together result in the formation of N_2 and O while consuming N atoms. The newly formed O atoms again recombine as per reaction (2) to form O_2 molecules, which initiates reaction (5). Thus, the above three reactions constitute a chain mechanism, where O_2 molecules act as a catalyst in the conversion of N atoms to N_2 molecules with no net effect on O_2 and O concentration. This reaction mechanism is similar to that described by Park[6] for expanding nozzle flows. The chain reactions will cease when nitrogen recombination is complete. In the absence of N atoms, only recombination of oxygen will occur. At the current conditions, N atoms are not completely depleted, and therefore the concentrations of O_2 and O do not change. Note that $R_2 \neq R_4 \neq R_5$, with R_4 and R_5 attaining large local values in the immediate vicinity of wall. An imbalance in these three reactions produces local peaks in the source terms of O, O_2 and NO in the region $0 < l/\delta < 0.004$. However, there is no appreciable effect of these locally high values of the source terms on the corresponding species mass fractions (see Fig. 5(b)).

The conversion of N atoms to N_2 molecules in the boundary layer occurs via the two competing reaction mechanisms described above. The first mechanism (R_3-R_4) comprises reactions (3) and (4), and is initiated by NO recombination. The second mechanism (R_2-R_5-R_4), consisting of reactions (2), (4) and (5), is initiated by O_2 molecules. The majority of the N_2 recombination occurs via the first mechanism. A preference for the R_3-R_4 mechanism can be explained by comparing the rate coefficients of NO and O_2 recombinations. The primary collision partners for these two reactions are N_2, N and O. The rate constants shown in Fig. 7 correspond to the case where the collision partner is an atom, and the temperature range spans

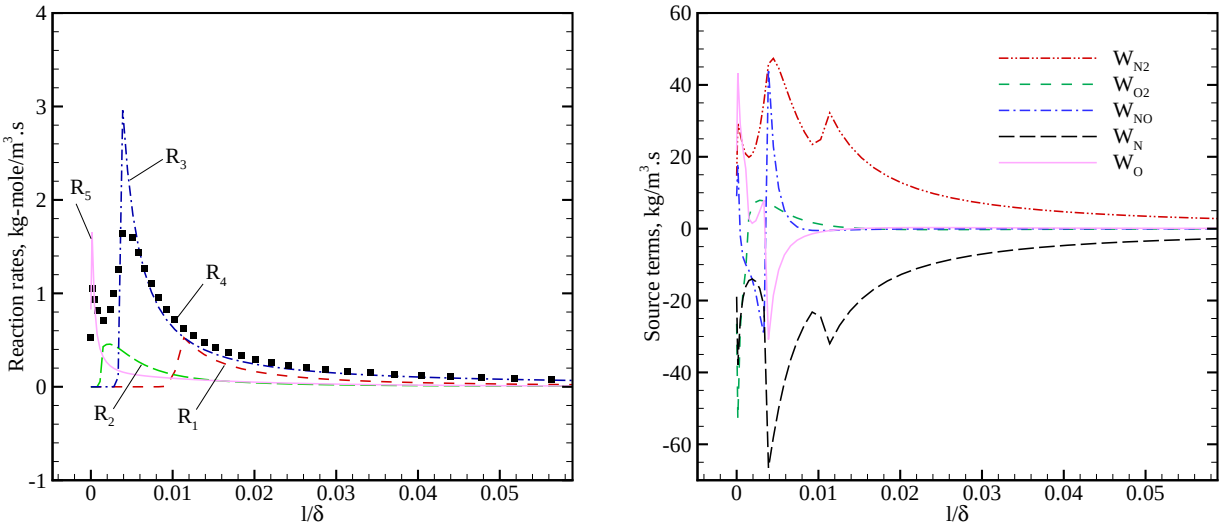

Figure 6: Variation of (a) reaction rates and (b) species source terms in the thermal boundary layer at the nose stagnation point.

the present boundary-layer conditions. The rate coefficient of NO recombination is higher than that of O_2 recombination, which indicates that NO recombination occurs at a faster rate than the latter. Hence, the R_3-R_4 mechanism initiated by NO molecules has a dominant contribution to N_2 formation. As N_2 recombination progresses, the concentration of N atoms decreases and leads to a sudden reduction in R_3 at $l/\delta = 0.004$ (see Fig. 6(a)). When NO molecules are not produced through reaction (3), O_2 recombination initiates the R_2-R_5-R_4 mechanism.

B. Altered reactivity in the boundary layer

Numerical simulations are performed by changing the rate constants of the five reactions, individually and in groups, to study their effect on the surface heat-transfer rate. The magnitude of reaction rates, source terms and extent of N_2 formation obtained in the new simulations are compared with those in the baseline solution presented above. The reaction rate constants are first altered only in the boundary layer to study their local effects. Solutions are then computed by changing the rate constants in the entire domain.

The rate constants of O_2 and NO recombination are varied initially, as these two reactions initiate the two competing N_2-recombination mechanisms. The corresponding stagnation point heat transfer rates are listed in Table 2. It is found that an increase in the rate constant of NO recombination enhances the heating rate significantly, and lowering the rate constants of this reaction decreases the surface heat flux. An increase in the O_2 recombination rate constant also leads to enhanced heating rate. However, the heat flux increment is lower than that obtained when NO recombination is enhanced. Further, decreasing the rate constant of O_2 recombination has minimal effect on the surface heat flux. The changes in gas chemistry due to altered reactivity in the boundary layer, and the consequent variation in gas properties and the surface heating rate, are explained below.

Figure 8(a) shows the magnitude of reaction rates when rsf = 10 for NO recombination. The reaction rates qualitatively match those observed in the baseline simulation, as shown in Fig. 6(a). The R_3-R_4 mechanism is dominant, and the corresponding rates are increased over their baseline values. An enhanced production of NO molecules leads to an increase in magnitude of the exchange reaction rate R_4. The rates of other reactions (R_2 and R_5) remain relatively unchanged from their respective values in the baseline simulation. The associated changes in Y_{N_2} and Y_N are shown in Fig. 8(b). Formation of N_2 in the boundary layer is enhanced due to an increased magnitude of R_3 and R_4. Mass fraction of N_2 reaches a value of 0.68 at the wall, whereas Y_N decreases to 0.08.

Figure 9 shows the reaction rates obtained for the case with rsf = 0.1 for NO recombination. The magnitude of R_3 is greatly reduced compared to the baseline simulation, whereas the magnitude of R_2 is

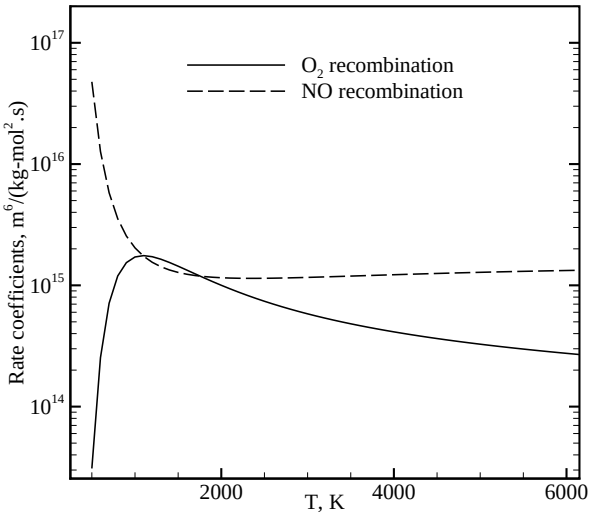

Figure 7: Comparison of baseline rate constant for O_2 and NO recombination.

Reaction	rsf	heating rate (W/cm^2)	% change
Baseline	1.0	80.49	-
$NO + M \rightleftharpoons N + O + M$	10.0	114.18	41.86
$O_2 + M \rightleftharpoons 2O + M$	10.0	101.56	26.18
$N_2 + O \rightleftharpoons NO + N$	10.0	80.99	0.5
$NO + O \rightleftharpoons O_2 + N$	10.0	81.93	1.8
$N_2 + M \rightleftharpoons 2N + M$	10.0	82.2	2.12
Five reactions	10.0	118.60	47.34
$NO + M \rightleftharpoons N + O + M$	0.1	61.57	-23.51
$O_2 + M \rightleftharpoons 2O + M$	0.1	78.25	-2.78
$N_2 + O \rightleftharpoons NO + N$	0.1	80.17-	-0.4
$NO + O \rightleftharpoons O_2 + N$	0.1	79.44	-1.3
$N_2 + M \rightleftharpoons 2N + M$	0.1	79.77	-0.9
Five reactions	0.1	51.75	-35.71

Table 2: Stagnation point heating rate obtained when the rate constants of reactions are altered. The percentage change is calculated with respect to the baseline heating rate value.

approximately equal to its baseline value. Note that the reduced NO recombination rate constant ($0.1\times k_{b_3}$) is lower than the O_2 recombination rate constant k_{b_2} (Fig. 10). O_2 recombination therefore proceeds faster than NO recombination for this case, and formation of N_2 primarily occurs via the R_2-R_5-R_4 mechanism throughout the boundary layer. The reaction rates R_4 and R_5 are also found to be lower in this case than their respective baseline values. Overall, N_2 formation in the boundary layer is suppressed. Mass fraction of N_2 attains a value of 0.36 at the wall, as compared to the baseline value of 0.49.

Figure 11 presents the magnitude of reaction rates obtained when rsf = 10 for O_2 recombination. An increase in k_{b_2} makes the O_2 recombination proceed at a faster rate than NO recombination (see Fig. 10). Thus, the second mechanism (R_2-R_5-R_4) is favored for the formation of N_2 molecules in this case. The reaction rates R_2, R_5 and R_4 increase by a factor of ten, as compared to their respective baseline values. The higher reaction rates enhance N_2 formation near the wall, and result in a higher concentration of N_2 in the boundary layer ($Y_{N_2} = 0.63$ at the wall). On the other hand, when k_{b_2} is decreased, the magnitude of R_2 decreases by ten times and this results in suppression of R_2-R_5-R_4 mechanism in the vicinity of wall. Compared to the R_3-R_4 mechanism, which has a dominant contribution to N_2 formation in this case, suppression of R_2-R_5-R_4 mechanism has negligible effect on the extent of recombination. Mass fraction of N_2 approaches 0.48 at the wall, as compared to 0.49 in the baseline solution.

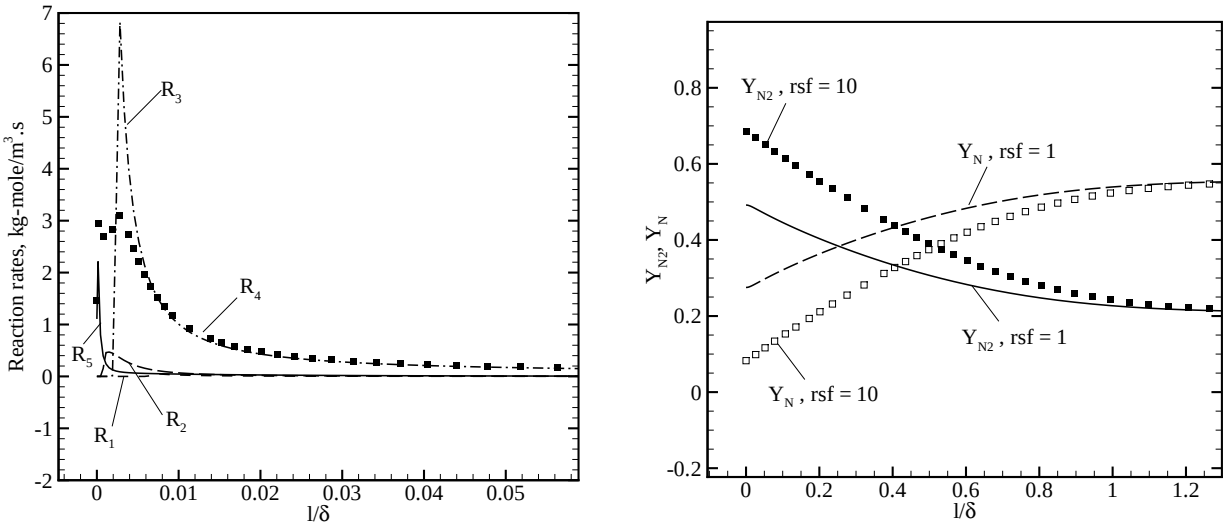

Figure 8: Variation of (a) reaction rates and (b) gas composition in the boundary layer, when rsf = 10 for NO recombination.

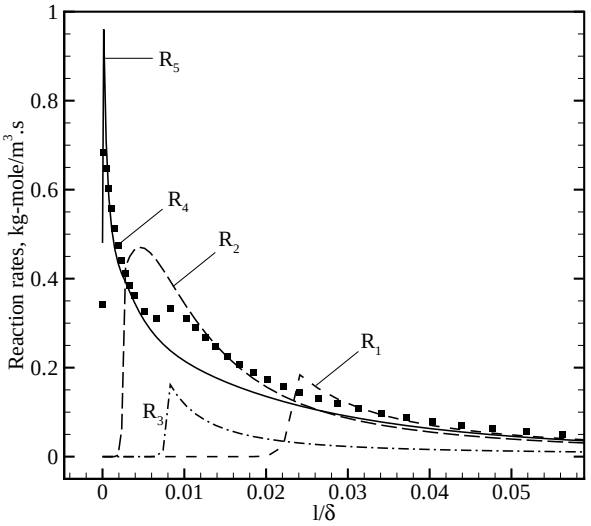

Figure 9: Magnitude of reaction rates when rsf = 0.1 for NO recombination.

Altering the rate constants of exchange reactions (4) and (5), and N_2 recombination reaction (1) independently has negligible effect on the stagnation point heating rate (see Table 2). The essential species required for N_2 formation are O_2 or NO. The reactions (1), (4) and (5) do not produce the above two species in the boundary layer. Hence, changing the reactivity of these three reactions does not alter the N_2 formation process. On the other hand, increasing (decreasing) the reactivity of either O_2 or NO recombination enhances (suppresses) the respective mechanisms of N_2 production. Thus, we can say that O_2 and NO recombination reactions are the rate limiting steps in the N_2 recombination process.

Next, we alter the rate constants of all five chemical reactions simultaneously in the boundary layer, and the corresponding reaction rates are shown in Fig. 12. In case of the reduced reactivity (rsf=0.1), the N_2 recombination process is similar to that observed in the baseline simulation (Fig. 6(a)), but the magnitude of all reaction rates is lower than their corresponding baseline values. The majority of recombination occurs via the R_3-R_4 mechanism, and the R_2-R_5-R_4 mechanism is active in the immediate vicinity of wall. The key element in the above chain reactions is availability of either NO or O_2 molecules. A decrease in the rate

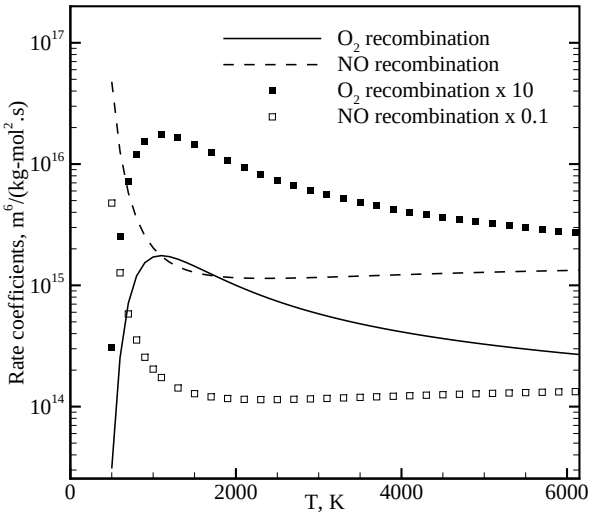

Figure 10: Comparison of altered rate constant for O_2 and NO recombination.

constants of O_2 and NO recombination reduces the formation of O_2 and NO molecules respectively, and this leads to a reduction of the exchange reaction rates R_4 and R_5. Thus, there is a marginal recombination of N atoms across the boundary layer (see Fig. 13), with $Y_{N_2} = 0.3$ at the wall.

Figure 12(b) plots the reaction rates across the boundary layer for the higher reactivity simulation (rsf = 10 for all reactions). The reaction mechanism R_2-R_5-R_4 is preferred in this case for the recombination of N atoms. The rates of the three reactions are enhanced significantly. An increase in the rate constants of O_2 recombination results in a higher availability of O_2 molecules. This, along with an increased rate constant k_{b_5}, enhances the magnitude of R_5 more than ten times, as compared to its baseline value. A higher R_5 increases the production of NO and O, which in turn leads to an increase in the magnitude of R_4. This results in higher level of N_2 and O. The newly created O atoms again recombine to form O_2 molecules, which accelerate the loop reactions further. Thus, the present N_2 recombination is a chain mechanism and an increase in one reaction rate recursively enhances the other dependent reactions. The net effect is a large increase in the N_2-level in the boundary layer (see Fig. 13). The mass fraction of N_2 reaches a value of 0.76 at the wall, which is 55% higher than the baseline value.

C. Effect on Surface Heat Flux

Increasing and decreasing the rate constants of five reactions simultaneously result in a stagnation point heating rate of 117.87 and 44.20 W/cm^2 respectively. The heating-rate enhancement obtained when all the reaction rates are increased is higher than that obtained when rate constants of O_2 or NO recombinations are increased individually (see Table 2). This is because all reactions in the boundary layer proceed in the exothermic direction and they favor the recombination process. An increase in the rate constant of an individual reaction therefore enhances N_2 formation, and increasing the rates of all five reactions simultaneously leads to the formation of N_2 to the highest extent. The corresponding heat release is highest when all the reaction rates are increased and it enhances the surface heat flux. On similar lines, the heat released due to exothermic reactions is minimum when the rates of all five reactions are decreased. The corresponding heat flux is lower than those obtained by reducing the rate constants of individual reactions.

The heat flux to the vehicle surface is a function of near-wall gas temperature and the mixture conductivity. The change in the heat flux due to varying reaction rates can, therefore, be expressed in terms of the changes in the thermal conductivity and the gas temperature adjacent to wall T_2.

$$\frac{\triangle q}{q} = \frac{\triangle \kappa}{\kappa} + \frac{\triangle T_2}{T_2 - T_w} \tag{9}$$

where higher-order terms are neglected. A budget of Eq. (9) for the stagnation point heat flux for the higher and lower reactivity simulations is shown in Table 3, where the changes are calculated with respect to the

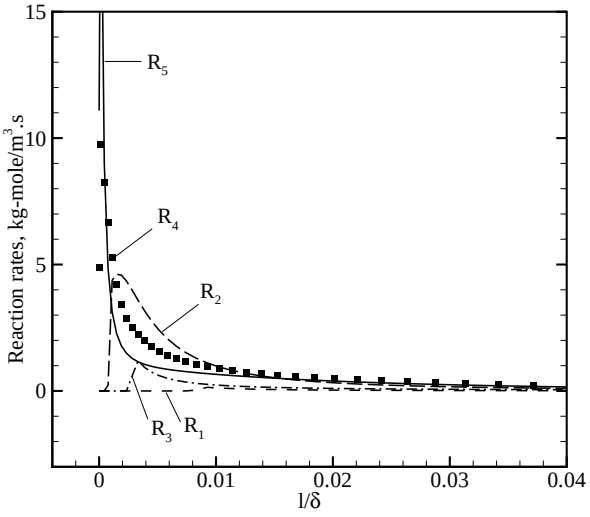

Figure 11: Magnitude of reaction rates when rsf = 10 for O_2 recombination.

% change	rsf = 10	rsf = 0.1
$\triangle\kappa/\kappa$	-16.79	9.42
$\triangle T_2/(T_2 - T_w)$	76.00	-49.85
$\triangle q/q$	46.46	-45.08

Table 3: Contribution of $\triangle\kappa/\kappa$ and $\triangle T_2/(T_2 - T_w)$ to $\triangle q/q$ in the higher (rsf = 10) and lower (rsf = 0.1) reactivity cases at the nose stagnation point.

baseline simulation values. Enhancing the reactivity (rsf = 10) increases the gas temperature in the near-wall region by 76%, and the gas temperature decreases by about 50% when the reaction rates are reduced (rsf = 0.1).

At the current boundary-layer conditions, the relative magnitude of thermal conductivity among the species is:

$$\kappa_{\mathrm{N}} > \kappa_{\mathrm{O_2}} > \kappa_{\mathrm{NO}} > \kappa_{\mathrm{N_2}} > \kappa_{\mathrm{O}} \tag{10}$$

Molecular nitrogen has lower thermal conductivity than its atomic counterpart. Increasing (decreasing) the reaction rates results in a higher (lower) mass fraction of N_2, thereby reducing (enhancing) the overall mixture conductivity. It decreases by 16.79% for the higher reactivity simulation and increases by 9.42% in the lower reactivity case. The changes in conductivity are opposite to those in the near-wall gas temperature. The heat release or the temperature effect is found to be the dominant contribution to the surface heat transfer rate. The net effect is an enhancement in the stagnation point heating rate by 46.46% when the rate constants are increased, and a reduction in the heat flux by 45.08% when the rate constants are decreased. Note that the changes in thermal conductivity and temperature do not match the net change in q as per Eq. (9), because of the contributions of higher-order terms that are neglected in the analysis.

The equilibrium gas composition for the prescribed wall temperature and the computed wall pressure is $Y_{\mathrm{N_2}} = 0.767$, $Y_{\mathrm{O_2}} = 0.233$ and $Y_{\mathrm{NO}} = Y_{\mathrm{N}} = Y_{\mathrm{O}} = 0.0$. In the present computations with the baseline rate constants, $Y_{\mathrm{N_2}}$ and $Y_{\mathrm{O_2}}$ values are 0.492 and 5×10^{-5} respectively at the nose stagnation point. The gas composition is far from its local equilibrium state. An increase in chemical rate constants takes the gas closer to the equilibrium state by promoting the recombination reactions. The mass fraction of N_2 for the higher reactivity case is 0.76 (see Fig. 13), *i.e.* N_2 recombination is almost complete. On the other hand, $Y_{\mathrm{O_2}}$ approaches a value of 0.002 at the wall in the higher reactivity simulation. There is negligible O_2 formation in spite of the enhanced reactivity. This is because any O_2 molecule formed is used up by the subsequent reactions in the R_2-R_5-R_4 mechanism leading to N_2 formation. Any change in O_2 is expected to be seen only when N_2 recombination is complete and the chain mechanism is disrupted because of non-availability

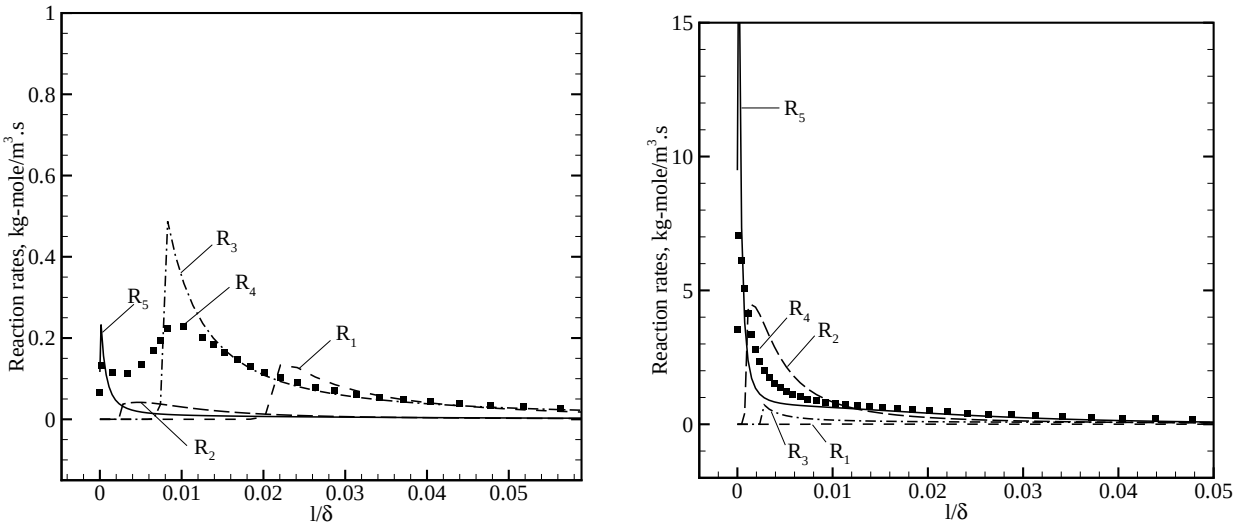

Figure 12: Magnitude of reaction rates when (a) rsf = 0.1, and (b) rsf = 10 for all reactions.

of N atoms.

D. Increased Reactivity in the Entire Domain

The foregoing analysis is based on altering the chemical reaction rates in the thermal boundary layer adjacent to the vehicle wall. By comparison, the results presented below are obtained when the rate constants are increased (rsf = 10) for all five reactions uniformly over the entire computational domain. Figure 14(a) presents the variation of T and T_v along the stagnation streamline obtained from the baseline simulation and the rsf = 10 simulation. The higher reactivity solution yields a lower shock stand-off distance by 7.69%. This is due to a higher amount of dissociation at the shock wave in the increased reactivity simulation. The enhanced rate constants also result in reduced peak values of T and T_v by about 3600 and 6600 K respectively, as compared to the baseline solution.

There is a large difference between the translational temperatures obtained in the two solutions in the vicinity of the shock wave, and the difference reduces as we go downstream. Both solutions approach $T = 6300$ K close to the boundary-layer edge. Comparison of vibrational temperatures obtained from the two cases shows a similar trend. In both the baseline and higher reactivity solutions, the gas is in a thermal non-equilibrium state in the majority of the shock layer, and it reaches thermal equilibrium ($T = T_v$) close to the boundary-layer edge. Thus, all the temperatures plotted in Fig. 14(a) attain a value close to 6300 K at the edge of the thermal boundary layer.

Figure 14(b) compares Y_{N_2} along the stagnation streamline for the two solutions. Similar to the temperature plot, there is a noticeable difference between Y_{N_2} values in the post-shock region. In the higher reactivity case, the chemical reactions equilibriate immediately downstream of the shock at $x \simeq$ -0.03 m, and the composition remains approximately constant thereafter. By comparison, there is a slower decrease in Y_{N_2} behind the shock in the baseline simulation, and the gas approaches chemical equilibrium close to boundary-layer edge ($x \simeq$ -0.01 m). Overall, the gas composition and temperatures obtained using higher rate constants match those in the baseline simulation at the boundary-layer edge, in spite of large differences in the vicinity of the shock wave.

The variation in Y_{N_2} in the thermal boundary layer is also shown in Figure 14(b). The mass fraction of N_2 obtained from the higher reactivity case reaches a higher value at the wall as compared to the baseline simulation. This is similar to that observed when the reaction rate constants are increased only in the boundary layer (see Fig. 13). The wall value of Y_{N_2} obtained from the two higher reactivity simulations (entire domain and boundary layer) are almost identical. The concentration of nitrogen atoms shows a similar trend. The mass fraction of other species, Y_{O_2}, Y_O and Y_{NO}, remain constant across the boundary layer, as observed in the baseline solution.

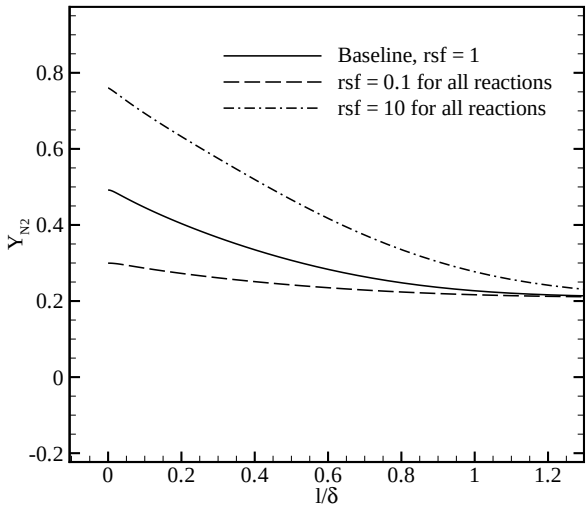

Figure 13: Variation of Y_{N_2} across the boundary layer for the baseline and the altered reactivity cases.

The stagnation point heating rate obtained from the higher reactivity simulation is 118.60 W/cm^2, which is 47.34 % higher than the baseline solution. The heating rate enhancement due to increased reactivity in the entire domain is close to that obtained when the reaction rate constants are altered only in the boundary layer. This is due to identical gas composition and temperatures across the boundary layer in the two higher reactivity simulations, as described above.

E. Decreased Reactivity in the Entire Domain

Next, simulation is performed with reduced rate constants for all five reactions in the entire domain. Figure 15 shows a comparison of N_2 mass fraction and temperatures along the stagnation streamline obtained from the baseline simulation and the lower reactivity simulation. Suppression of chemical reactions in the shock layer yields a shock stand-off distance that is larger by 34% than the baseline solution. The reduced dissociation rate results in a slower decrease in Y_{N_2} and an increase in the peak translational temperature (by 2000 K) at the shock. The peak vibrational temperature also increases by 6300 K, as compared to the baseline solution. Unlike the higher reactivity case (see Sec. III.D), the differences in T and Y_{N_2} between the lower reactivity and baseline solutions persist upto the boundary-layer edge. The effect of these variations on the heating rate is discussed below.

A comparison of Y_{N_2} across the thermal boundary layer of the two solutions show significant differences. With the reaction rates reduced over the entire domain, Y_{N_2} reaches a value of 0.31 at the wall, and is lower than the corresponding baseline value of 0.49, but close to the Y_{N_2} obtained when the reactivity is decreased only in the boundary layer (Fig. 15(a)). This is due to a compensating effect of lower dissociation at the shock and a lower degree of recombination in the boundary layer, when the reaction rates are altered in the entire domain.

The stagnation point heat flux obtained with reduced reactivity in the entire domain is 51.75 W/cm^2. It is lower than the baseline heating rate value and higher than that obtained when the rate constants are decreased only in the boundary layer. The heat flux at the surface is mainly determined by the amount of heat release in the boundary layer due to recombination reactions and by the boundary-layer edge temperature. The boundary-layer heat release is the main contributor to the difference observed between baseline heating rate and that obtained with the reduced rate constants in the entire domain. A lower heat release due to reduced exothermic reactions in the boundary layer leads to a lower heat flux by 35.71% as compared to the baseline value. On the other hand, the boundary-layer edge effect plays a dominant role while comparing the two lower-reactivity simulations. A higher boundary-layer edge temperature obtained when the reaction rate constants are reduced in the entire domain results in a higher heating rate by 17.08% as compared to that obtained when the reactions are suppressed only in the boundary layer.

In summary, the surface heat transfer rate is function of the competing effects in the boundary layer and

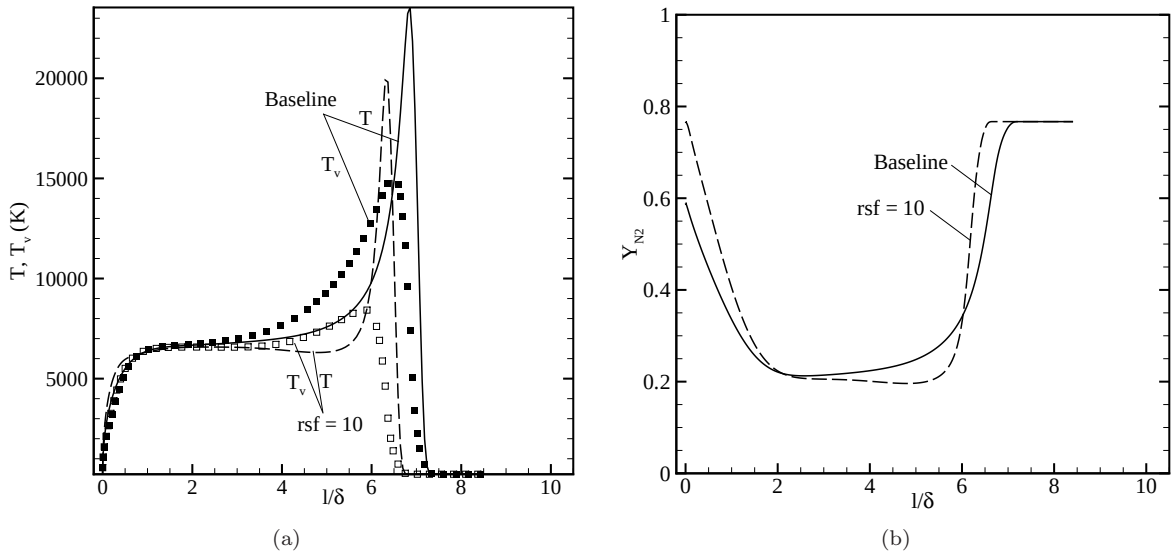

Figure 14: Changes in (a) T and T_v and, (b) Y_{N_2} along the stagnation streamline due to enhanced reactivity in the entire domain.

shock layer. The extent of exothermic reactions in the boundary layer determines the gas temperature and mixture conductivity in the immediate vicinity of the wall. On the other hand, the degree of dissociation in the shock layer affects the gas properties at the boundary layer edge, which in turn influence the heating rate.

IV. Comparison with Lower-Altitude Simulations

In our earlier paper,[5] we identified three critical factors that influence the sensitivity of surface heat flux to variation in chemical reaction rates. First, dominant chemical reaction(s) in the gas; second, chemical state of the gas–equilibrium, non-equilibrium or frozen; and third, extent of recombination in the boundary layer. A comparison of these factors in the lower-altitude (35 km) condition[5] and the present case (70 km altitude) is given below.

A higher stagnation enthalpy of the flow at the higher-altitude trajectory point results in dissociation of N_2 and O_2 at the bow shock, where as only O_2 is dissociated at the lower-altitude condition. Recombination of O atoms via O+O→O_2 is the dominant chemical activity in the boundary layer of the lower-altitude simulation. Hence, the stagnation point heat flux at 35 km altitude is sensitive only to the variation in O_2 recombination rate. By comparison, conversion of nitrogen atoms to molecules is the main chemical effect in the boundary layer of the higher-altitude flowfield. The mass fractions of O_2, O and NO remain constant across the boundary layer. The reactions participating in N_2 formation are O+O→O_2, N+O→NO and the two exchange reactions, and the surface heat flux is sensitive to changes in the rate constants of these reactions. The highest variation in the heating rate is observed when all the reaction rates are altered simultaneously.

At the 35 km altitude condition, gas density is high enough for the thermo-chemistry to equilibriate in the vicinity of the bow shock. Hence, the gas is in thermo-chemical equilibrium state in the majority of the shock layer. By comparison, freestream density at the 70 km altitude condition is lower by two orders of magnitude. The thermo-chemistry is therefore mostly in a non-equilibrium state in the shock layer, and approaches equilibrium close to the nose stagnation point. Therefore, increasing (decreasing) the reactivity leads to a higher (lower) amount of dissociation at the bow shock. Compared to the baseline simulation, the shock stand-off distance decreases when the reaction rate constants are increased, and vice-versa. On the other hand, the shock stand-off distance is relatively insensitive to variation in the chemical reaction rates at the lower-altitude condition. This is because of the prevailing chemical equilibrium in the shock layer such that altering the rate constants does not change the gas composition and its density appreciably.

In the lower-altitude simulation, O_2 recombination is almost complete in thermal boundary layer adjacent

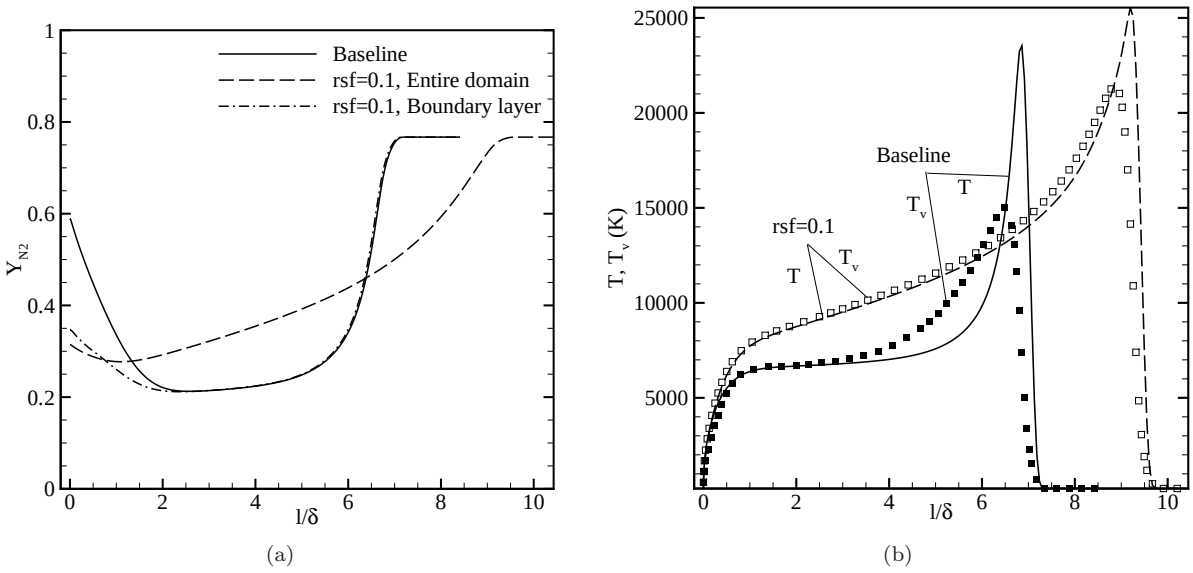

Figure 15: Changes in (a) Y_{N_2} and (b) T and T_v along the stagnation streamline due to decreasing rate constants in the entire domain.

to the stagnation point. Enhancing the rate constants has a marginal effect on the stagnation point heating rate (2%), where as decreasing the reaction rates reduces the heat flux appreciably (9%). At the higher-altitude trajectory point, the baseline reaction rates yield a partial recombination of N_2 in the boundary layer. Increasing the rate constants leads to additional recombination of N_2. The resulting heat release enhances the surface heat flux by a large fraction (47%). An opposite effect is observed when the rate constants are reduced, and the heating rate decreases by 36%. Though stagnation point heat flux is affected by variation in kinetic data at both altitudes, the sensitivity of the same is appreciably greater at the higher altitude condition. This is due to the higher degree of non-equilibrium in the flow at the 70 km altitude.

V. Conclusions

A re-entry flowfield at Mach 26.2 and 70 km altitude condition is numerically simulated, and the thermo-chemistry is analyzed along the stagnation stream line. At this condition, dissociation of N_2 and O_2 occurs in the shock layer, with partial recombination of nitrogen atoms at the wall. Two reaction mechanisms are identified for N_2 recombination. The first mechanism consists of NO recombination and the exchange reaction NO+N→N_2+O. The second mechanism is initiated by O_2 recombination, and is followed by the exchange reactions, O_2+N → NO+O and NO+N → N_2+O. The net effect of these reactions is to convert N atoms into N_2 molecules. There is no change in the concentrations of O, O_2 and NO.

Simulations are next performed by selectively altering the reaction rates in different regions. These controlled numerical experiments highlight interesting aspects of the thermo-chemistry and its effect on the flowfield predictions.It is found that the changes in the heating rate due to variation of chemical reaction rate constants depends on the relative contribution of the corresponding reaction mechanism towards N_2 recombination in the boundary layer. The heat flux is most sensitive to the rate-limiting reactions, namely, the NO and O_2 recombination rates. In general, increasing the rate constants of individual reactions enhances the heat transfer rate and vice versa. Highest heat flux is obtained when all the rate constants are increased simultaneously in the boundary layer.

Shock layer thermo-chemistry further affects the surface heat flux by altering the boundary-layer edge conditions. Specifically, reducing the dissociation rate constants leads to a hotter shock layer. This increases the boundary-layer edge temperature, which tends to elevate the heating rate. This is opposite to that observed in the boundary layer, where reducing the rate constants of the exothermic reactions tends to lower the surface heat flux. Comparison with lower-altitude simulations shows that the stagnation point heat flux at the current condition is significantly more sensitive to the variations in kinetic data. This is because of the low gas density at the higher-altitude trajectory point, which leads to a higher degree of thermo-chemical

non-equilibrium in the flowfield.

VI. Acknowledgment

The authors thank Indian Space Research Organization (ISRO) for supporting this research under the RESPOND program. The authors would like to acknowledge Rajhansa Sridhara, a student at IIT Bombay, for his assistance in the shock-grid alignment simulations presented in this paper.

References

[1] Candler, G.V., and Olejniczak, J., "Nitrogen Dissociation Rates in Complex Hypersonic Flows," AIAA Paper 1997-2500, 1997.

[2] Bertin, J.J., *Hypersonic Aerothermodynamics*, AIAA Education Series, 1994, pp. 143-149.

[3] Reddy, D.S.K., and Sinha, K., "Effect of Chemical Reaction Rates on High-enthalpy Flow Prediction Around a Re-entry Capsule," Under Review, *Journal of Thermophysics and Heat Transfer*, June 2011.

[4] Wright, M.J., Prabhu, D.K., and Martinez, E.R., "Analysis of Apollo Command Module Afterbody Heating Part I: AS-202," *Journal of Thermophysics and Heat Transfer*, Vol. 20, No. 1, January-March 2006, pp. 16-30.

[5] Reddy, D.S.K., and Sinha, K., "Effect of Chemical Reaction Rates on Aero-heating Predictions of Re-entry Flows," *Journal of Thermophysics and Heat Transfer*, Vol. 25, No. 1, January-March 2011, pp. 21-33.

[6] Park, C., *Non-Equilibrium Hypersonic Aerothermodynamics*, A Wiley-Interscience Publication, New York, 1990, pp. 35, 255-268 and 326.

[7] Bose, D., and Wright, M.J., "Uncertainty Analysis of Laminar Aeroheating Predictions for Mars Entries," AIAA Paper 2005-4682, 2005.

[8] Palmer, G.E., "Uncertainty Analysis of CEV LEO and Lunar Return Entries," AIAA Paper 2007-4253, 2007.

[9] Tchuen, G., and Zeitoun, D., "Effects of Chemistry in Nonequilibrium Hypersonic Flow Around Blunt Bodies," *Journal of Thermophysics and Heat Transfer*, Vol. 23, No. 3, July-September 2009, pp. 433-442.

[10] Blottner, F.G., Johnson, M., and Ellis, M., "Chemically Reacting Viscous Flow Program for Multi-component Gas Mixtures," Sandia Laboratories Report No. SC-RR-70-754, Albuquerque, New Mexico, 1971.

[11] Vincenti, W.G., and Kruger, C.H., *Introduction to Physical Gas Dynamics*, Krieger Publications, Malabar, Florida, 1986, pp. 407.

[12] Wilke, C.R., "A Viscosity Equation for Gas Mixtures," *Journal of Chemical Physics*, Vol. 18, 1950, pp. 517-519.

[13] MacCormack, R.W., and Candler, G.V., "The Solution of the Navier-Stokes Equations Using Gauss-Siedel Line Relaxation," *Computers and Fluids*, Vol. 17, No. 1, 1989, pp. 135-150.

[14] Wright, M.J., Candler, G.V., and Bose, D., "Data-Parallel Line Relaxation Method for the Navier-Stokes Equations," *AIAA Journal*, Vol. 36, No. 9, 1998, pp. 1603-1609.

[15] Pasha, A.A., and Sinha, K., "Shock-unsteadiness Model Applied to Oblique Shock wave/turbulent Boundary-layer Interaction," *International Journal of Computational Fluid Dynamics*, Vol. 22, No. 8, September 2008, pp. 569-582.

[16] Pasha, A.A., and Sinha, K., "Shock-unsteadiness Model Applied to Hypersonic Shock-wave/turbulent Boundary-layer Interactions," *Journal of Propulsion and Power*, accepted, June 2011.

[17] Reddy, D.S.K., and Sinha, K., "Hypersonic Turbulent Flow Simulation of FIRE II Reentry Vehicle Afrerbody," *Journal of Spacecraft and Rockets*, Vol. 46, No. 4, July-August 2009, pp. 745-757.

[18] Saunders, D., Yoon, S., and Wright, M., "An Approach to Shock Envelope Grid Tailoring and Its Effect on Reentry Vehicle Solutions ," AIAA Paper 2007-207, 2007.

[19] Nompelis, I., and Candler, G.V., "Investigation of Hypersonic Double-Cone Flow Experiments at High Enthalpy in the LENS Facility," AIAA Paper 2007-203, 2007.